ECS Transactions, 63 (1) 113-128 (2014)
10.1149/06301.0113ecst ©The Electrochemical Society

Comparative Study of Different Alkali (Na, Li) Titanate Substrates as Active Materials for Anodes of Lithium - Ion Batteries

S. Chauque[a], C. B. Robledo[b], E. P. M. Leiva[b], F. Y. Oliva[a] and O. R. Cámara[a]

[a]INFIQC – Departamento de Físico Química,
[b]INFIQC – Departamento de Matemática y Física,
Facultad de Ciencias Químicas, Universidad Nacional de Córdoba,
Ciudad Universitaria X 5000 UHA, Córdoba, Argentina

The relationship between structure and lithium storage capacity of different titanate samples as anode materials for lithium-ion batteries is discussed. $Li_4Ti_5O_{12}$, $Na_2Ti_3O_7$ and $Na_2Ti_6O_{13}$ were synthesized by solid-state reaction. The structure, surface and morphology of the samples were characterized by SEM, XRD and RAMAN spectroscopy. The electrochemical performance was studied by galvanostatic charge-discharge cycling, cyclic voltammetry, electrochemical impedance spectroscopy and rate capability. The lithium titanate presented the highest capacity of the three electrodes, together with the most reversible potential plateau at 1.6 V vs. Li^+/Li^0 and the best response in rate capability. Apparent diffusion coefficients of Li^+ ions into the titanate matrices were obtained, showing the highest value for the lithium titanate compound. Between both sodium titanates, $Na_2Ti_6O_{13}$ presented the highest specific capacity and the best discharge retention.

Introduction

In the past few years, the use of renewable energy resources as well as more efficient energy storage systems has been favored topics in the agenda of most influential governments. A sustainable energy system is being demanded by modern society due mainly to global warming effects, the elevated price of oil and contamination produced by fossil fuels. This situation has driven in the area of scientific investigation a search for improved electrochemical storage systems that can safely store energy from sustainable sources, such as wind and solar power.

The use of portable electronic devices has been feasible thanks to the technology of lithium-ion batteries (LIB). They were first commercialized by Sony in 1991, consisting of a graphite anode and a layer oxide cathode and are still being used today. The energy storage at an average voltage of 3.8 V is five times higher than lead-acid batteries (1). They have the advantage of lower weight, higher energy density and faster charge and discharge rates, compared to other similar technologies. Even though they are the main batteries employed in portable electronics, it is important to attend several issues regarding safety, and to improve its energy storage capacity in order to be used in electric vehicles. Graphite and related compounds have a fragile structure and incorporate lithium at a potential around lithium metal deposition. Other similar alternatives do not show a well defined lithiation potential so that the use of better and safer anodes is necessary (2, 3). Lithium titanate, $Li_4Ti_5O_{12}$, is one of the best candidates for anode materials at the

moment for safer LIB for many reasons: lithium insertion process takes place at a higher potential than graphite, minimizing the decomposition of the solvent employed and consequently the formation of solid electrolyte interface (SEI). Also, it is a "zero-strain" material with only a 0.2% of change in cell volume when Li^+ ions are intercalated/de-intercalated (4). Even though this material and other related materials, such as TiO_2, TiO_2-B and hydrogen titanates have been extensively studied and characterized as lithium storage material (5–9), other family related compounds as sodium titanates have received less attention. In the present study, we focus on the preparation and structural characterization of Li and Na titanates with layered structure, and the electrochemical investigation of lithium insertion properties of these materials.

Experimental

Active material synthesis

All titanate samples were prepared by solid-state reaction using the corresponding alkali metal carbonates (Li, Na) and TiO_2 anatase as raw materials, to obtain about 2 g of the desired titanates. Lithium titanate and two different sodium titanates were synthesized with the following stoichiometry: $Li_4Ti_5O_{12}$, $Na_2Ti_3O_7$ and $Na_2Ti_6O_{13}$. The synthesis reactions are represented in the following equations:

$$5\,TiO_2 + 2\,Li_2CO_3 \rightarrow Li_4Ti_5O_{12} + 2\,CO_2 \quad [1]$$

$$3\,TiO_2 + Na_2CO_3 \rightarrow Na_2Ti_3O_7 + CO_2 \quad [2]$$

$$6\,TiO_2 + Na_2CO_3 \rightarrow Na_2Ti_6O_{13} + CO_2 \quad [3]$$

The reagents were mixed at stoichiometric ratio during 20 min in agate mortar, along with acetone to favor the mixing process. For the case of the reaction represented in equation 1, lithium carbonate was added in a 10% excess, due to the volatility of Li_2O (10). Subsequently, they were annealed applying a heating ramp of 2 °C/min from ambient temperature up to different temperatures and holding periods: ($Li_4Ti_5O_{12}$) 950 °C for 24 h, ($Na_2Ti_3O_7$) 800 °C for 20 h and ($Na_2Ti_6O_{13}$) 1000 °C for 1 h (10–12). After the annealing process a cooling ramp was set at 5 °C/min. In all cases a fine white powder was obtained and grounded in an agate mortar. All samples were kept in a humidity free ambient before use.

Structural characterization

The structure of the samples was analyzed by X-ray powder diffraction (XRD) using Cu Kα radiation (λ=1.5418 Å), measured with a PANalytical X'Pert PRO diffractometer. The XRD patterns where obtained in 2θ range from 10° to 90°, with 0.02° steps and a counting time of 10 s. The crystalline structures were identified using High Score software. Rietveld structure refinements of the XRD patterns were performed with the FULLPROF program, using the Inorganic Crystal Structure Database (ICSD).

Raman spectra were recorded with RAM HR HORIBA JOBIM YVONE equipment using a 514 nm excitation line of an Ar^+ ion laser at room temperature. A total of 10 scans were averaged for each sample with an exposition time of 10 s.

The microstructure of the samples was examined by Scanning Electron Microscopy (SEM) in a FE-SEM Σigma Microscope, using an accelerating voltage of 8 kV at a working distance of 8.5 mm with a secondary electron detector.

Electrochemical characterization

Three-electrode T-cells Swagelok type were used for all electrochemical measurements. They were assembled inside a glovebox chamber (MBraun MB10 compact), in Ar atmosphere with concentration of O_2 and H_2O less than 0.5 ppm.

The working electrodes were prepared by a mixture of the active alkali-titanate material, polyvinylidene fluoride (PVDF) binder and conductive carbon black (Timcal Super P) in a weight ratio of 80:10:10 respectively, dispersed in N-methyl-2-pyrrolidone solvent. The resulting slurries were casted onto a 15 μm thick copper foil, dried in oven at 80 °C for 24 h and pressed applying 10 ton cm^{-2}. The total mass of the film coatings was approximately 1.5-3.0 mg cm^{-2} depending of the titanate material. The coated foils were punched into 8 mm diameter disks to obtain the working electrode and dried at 80 ºC overnight under vacuum before introducing them in the glovebox for cell assembling. Metallic lithium was used as reference and counter electrodes (10 mm diameter disks) and fiberglass disks were used as spacer between the three electrodes. All the potential values reported hereafter are referred to Li^+/Li^0 couple standard potential. The working solution consisted of ethylene carbonate (EC) and dimethyl-carbonate (DMC) solvent mixture (1:1 by mass) containing 1M $LiPF_6$ salt as electrolyte. Otherwise specified, the chemicals were obtained from Sigma-Aldrich without further purification.

All electrochemical measurements, such as galvanostatic charge-discharge (GCD) cycles, cyclic voltammetry (CV), electrochemical impedance spectra (EIS) and rate capability (RC) experiments were performed with a CH Instruments 660C Potentiostat-Galvanostat, at room temperature.

For each working electrode, ten GCD cycles were performed at a current of C/2 within the range of 3.0 and 1.0 V in order to analyze the specific capacityof the different anode materials, expressed as mAh g^{-1} in terms of mass of active material. Following GCD cycles, CV experiments were performed on each electrode at different scan rates between 5.0 to 0.05 mV s^{-1} within the previously mentioned voltage range. After the CV experiments, an additional GCD cycle was performed interrupted by EIS measurements at selected potentials corresponding to different states of the charge (SOC) and discharge (SOD) process (50 and 100% SOC; 50 and 100% SOD). Each EIS spectra were recorded in the 10 kHz-10 mHz frequency range applying a perturbation of ± 5 mV amplitude.

Finally, RC experiments were performed with the same cut-off potentials as the GCD cycles applying a charge current of C/2 while the discharge currents were set at C/2, C, 2C, 5C and 10C consecutively.

Results and Discussion

Structural Characterization

Figure 1A shows the XRD patterns of the synthesized titanates samples. The patterns present typical peaks referenced by ICSD #75711, 15463 and 23877 for $Li_4Ti_5O_{12}$, $Na_2Ti_3O_7$ and $Na_2Ti_6O_{13}$, respectively. Rietveld refinement results for each pattern are included in the figure. XRD diffraction pattern of $Li_4Ti_5O_{12}$ reveals a face-centered cubic spinel structure with a space group of $Fd\bar{3}m$. Peaks corresponding to possible impurities such as rutile TiO_2 or a pure phase of Li_2O were not observed. $Na_2Ti_3O_7$ and $Na_2Ti_6O_{13}$ patterns present a monoclinic structure with a space group of P21/m and C2/m respectively. For the $Na_2Ti_3O_7$ sample, impurity peaks corresponding to a second titanate phase were observed and identified as 4% of $Na_2Ti_6O_{13}$. Finally, for $Na_2Ti_6O_{13}$, few traces of a second phase of rutile TiO_2 were found (3%).

The lattice parameters obtained by Rietveld refinement for all compounds are shown in Table I and they are in good agreement with those described in S. Huang *et al.* (10) and R. Dominko *et al.*(13).

TABLE I. Unit cell parameters refined by Rietveld analysis for the three titanate samples.

Sample	*A* (Å)	*b* (Å)	*c* (Å)	*β* (°)	Unit cell volume (Å^3)
$Li_4Ti_5O_{12}$	8.3547(4)	8.3547(4)	8.3547(4)	90.0000	583.2
$Na_2Ti_3O_7$	8.5849(4)	3.8042(9)	9.1418(9)	101.5762(9)	299.3
$Na_2Ti_6O_{13}$	15.1014(5)	3.7408(1)	9.1644(3)	99.0654(5)	517.7

Figure 1B shows the crystal structure representation for $Li_4Ti_5O_{12}$, where the *b* axis is coming out of the plane. Continuous channels can be observed, in between four oxygen ions (marked with an arrow in the figure) that could allow a possible lithium ion pathway for diffusion. Due to the face-centered cubic structure that it presents, the Li^+ ion can be inserted in any direction, presenting anisotropic effect that could result in an increase of the storage capacity for this material, compared to the other titanates, which do not present this kind of structure. In the case of $Na_2Ti_3O_7$ (Figure 1C), along the *b* axis, small channels between oxygen and sodium ions can be observed. Nonetheless, the repulsion with the Na^+ ions could not be beneficial for Li^+ ions to be stored in this material. In the other directions, not shown in the picture, a more compact structure can be observed. This fact may difficult the Li^+ ion diffusion. Figure 1D shows the crystal structure representation for $Na_2Ti_6O_{13}$ where two different channels in the left upper corner can be observed: a small rhombic channel between oxygen ions in the corner of the unit cell and a big quasi-rectangular channel delimited by two sodium ions (both marked with arrows in the figure). Both can offer two types of sites for lithium insertion and diffusion. From Figures 1 A, B and C it was possible to establish that all the unit cells contained two unit formula of each titanate compounds, and using the cell unit volume reported in Table I, theoretical gravimetric density values of 2.618; 3.476 and 3.348 g cm^{-3}, for $Li_4Ti_5O_{12}$, $Na_2Ti_6O_{13}$ and $Na_2Ti_3O_7$ active materials respectively, was calculated.

The phase purity of the synthesized titanate samples was also analyzed by Raman spectroscopy (Figure 2). The spectra for the titanate samples presented different features depending on the material. For $Li_4Ti_5O_{12}$, the broad peaks with maxima at 234.6, 269.1, 340.6, 430.3 and 673.7 cm^{-1} wavenumbers are in concordance with the vibration modes of the spinel structure ($A_{1g} + E_g + 3F_{2g}$), reported in (14, 15). The spectra of the sodium titanates are in excellent agreement with those reported by E. Bamberger *et al*. (12). The spectrum of $Na_2Ti_6O_{13}$ is dominated by lower frequency bands, which are very strong and well resolved. The bands from both titanates spectra around 660 and 680 cm^{-1} are due to the Ti-O-Ti stretch in edge shared TiO_6 octahedra. The bands at approximately 300 cm^{-1}, correspond to stretching vibrations between sodium and oxygen ions (16). Thus, the Raman and XRD results show the formation of highly crystalline phases of titanate compounds and a low amount of impurities for each sample.

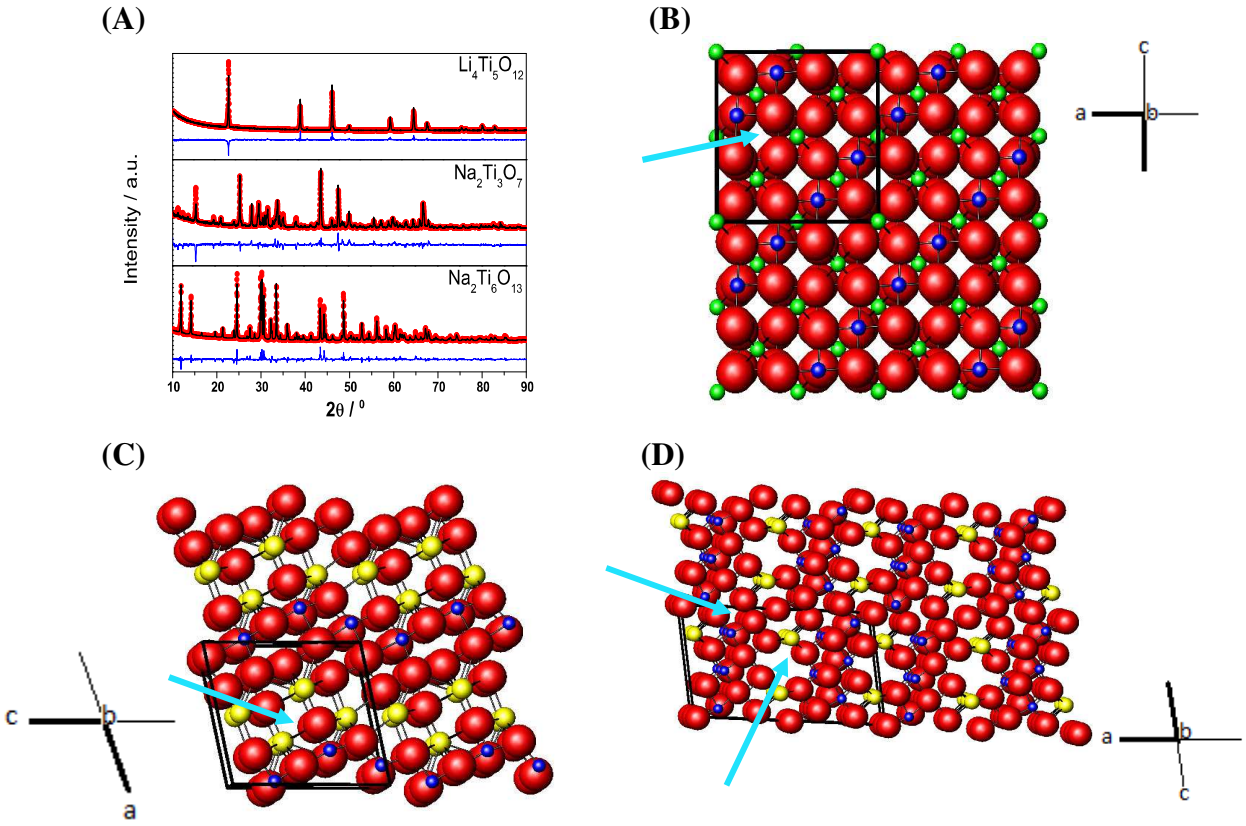

Figure 1. (A) XRD patterns of the three samples (red points) and Rietveld fitting (full black line). The difference curve is shown underneath each pattern in full blueline. (B-D) represents the schematic structure representations for $Li_4Ti_5O_{12}$, $Na_2Ti_3O_7$ and $Na_2Ti_6O_{13}$, respectively, reconstructed from the atoms positions obtained by the Rietveld analysis (four replicated unit cells). The black frame corresponds to the unit cell for each titanate sample and the light blue arrows indicates the possible diffusion channels for lithium ions as discussed in the text of the manuscript. Color code for atoms: Blue: Ti, Yellow: Na, Red: O, Green: Li.

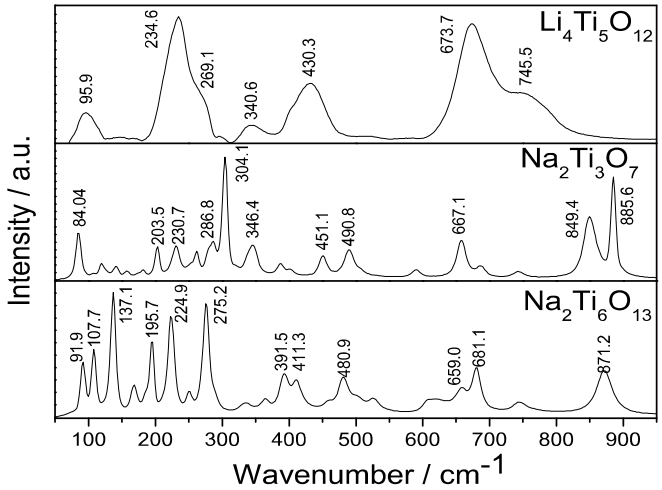

Figure 2. Raman spectra for the three titanates samples.

The morphology of the powder samples was analyzed by SEM (Figure 3). The images of the samples revealed that in all three cases the starting spherical anatase particles, shown in Figure 3A, were fully transformed into another material, at the highest temperature synthesis processes. The image of $Li_4Ti_5O_{12}$ (Figure 3B) shows that the material has a macro-porous structure. At higher magnifications, a well-crystallized material with a particular stepped pattern is revealed (shown in the inset). Both sodium titanates presented in Figures 3C and 3D show a random filamentous structure of different sizes distributed all over the samples, being for $Na_2Ti_3O_7$ mainly needle-like structures, while for $Na_2Ti_6O_{13}$ rod-like structures occur of approximately 200 nm long. Both samples also show a porous structure. From these SEM micrographs (and others do not shown here) it was possible to assign an "average" particle size as representative of each titanate materials. These representative particle sizes were (diameter): 16 μm for $Li_4Ti_5O_{12}$ and $Na_2Ti_6O_{13}$, and 20 μm to $Na_2Ti_3O_7$.

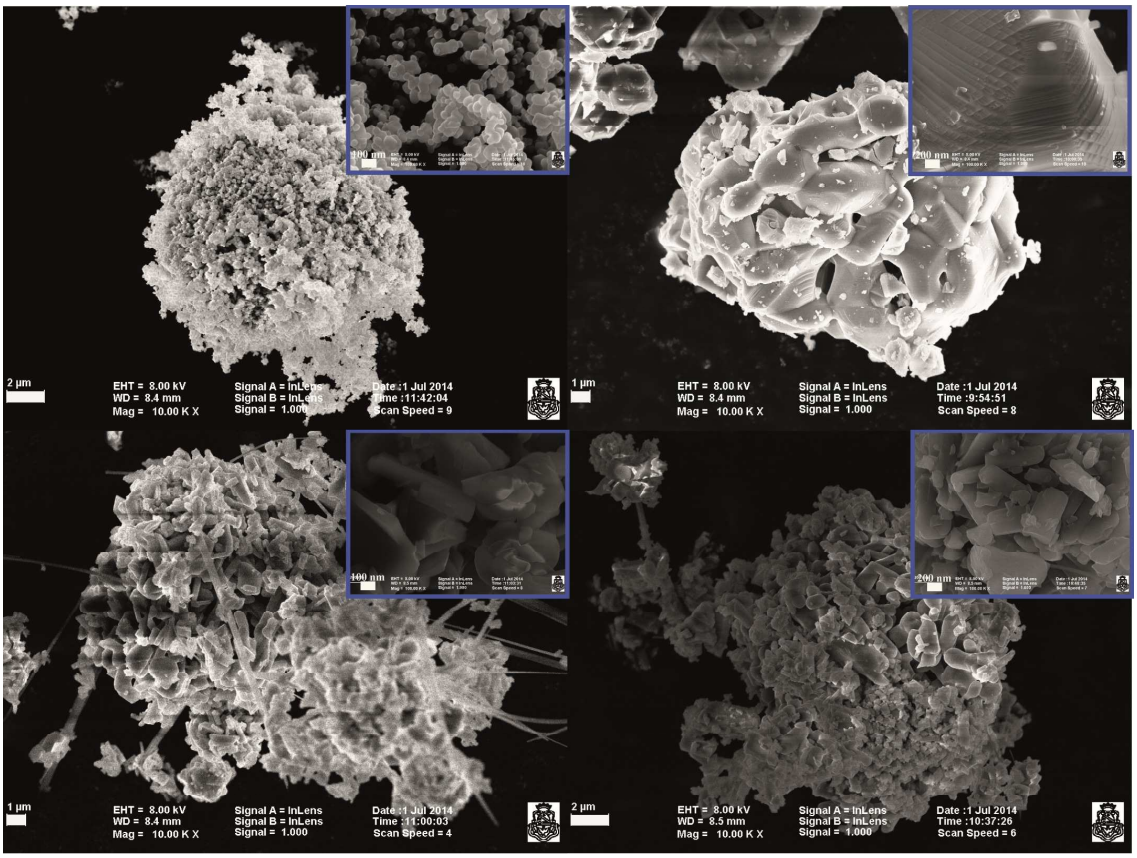

Figure 3. SEM images for: (A) TiO_2 anatase; (B) $Li_4Ti_5O_{12}$; (C) $Na_2Ti_3O_7$ and (D) $Na_2Ti_6O_{13}$. In the insets are amplifications of the images with a scale of 100 nm (A and C) and 200 nm (B and D).

Electrochemical Analysis

To study the electrochemical performance of the different titanates synthesized as active anode materials, the GCD curves for the tenth cycle were analyzed (Figure 4). Additional information can be obtained from the derivative curves of the GCD cycles. The differential capacity (Q_{diff}) is considered to be a measure of cell degradation and it is given by:

$$Q_{diff} = \frac{1}{Q_{max}} \frac{dQ}{dV} \quad [4]$$

Where $\frac{dQ}{dV}$ is the derivative of the amount of charge added (charge cycle) or removed (discharge cycle) with respect to the cell voltage, Q_{max} is the initial charge (or discharge) capacity obtained at C/2. When the differential capacity is plotted as a function of the cell voltage, the peaks of the resulting curves should be related to specific lithium insertion sites within the anode (17).

The electrode prepared with $Li_4Ti_5O_{12}$ as active material presents the highest capacity (approximately 100 $mAhg^{-1}$), compared to the sodium titanates studied, as shown in Figure 4. It has a reversible plateau at approximately 1.6 V, as evident in the differential capacity curves shown in Figure 5A. $Li_4Ti_5O_{12}$, presents the ideal behavior, where the peak position is kept unvaried along the life cycles.

It is well known that the Ti^{IV}/Ti^{III} redox couple works at 1.55 V, having as concomitant process the insertion/de-insertion of Li^+ ions in the channels of the spinel structure (4). Meanwhile, the insertion and de-insertion of lithium in the sodium titanates occur at a different potential. In the case of $Na_2Ti_3O_7$, the process takes place at a higher potential (approx. 1.7 V) than $Li_4Ti_5O_{12}$ and $Na_2Ti_6O_{13}$, and presents the lowest specific capacity. It is remarkable the shift in the peak position observed when the $Na_2Ti_3O_7$ electrode is subject to galvanostatic cycling. Such an effect is not observed in the other two cases. It has been proposed that the change in the potential of the peak is related to an increase in cell resistance, which results in a decreased capacity (18).

For $Na_2Ti_6O_{13}$, the insertion of Li^+ ion takes place at the lowest potential, presenting two small plateaus at 1.4 and 1.1 V, respectively (Figure 4). Previous articles have reported that lithium insertion in $Na_2Ti_6O_{13}$ is due to two phase reactions and a biphasic transition (13, 19). They observed that the reversible capacity became unexpectedly unstable when the electrode was cycled between 2.0 and 1.0 V vs. Li^+/Li^0 and they attributed this effect mainly to the low-potential stage of lithium insertion. Since the sites for accommodation of Li^+ ions were not known in this structure, Zhao *et al*. performed a first-principles study to understand such phenomenon (20). They established that Li^+ ions prefer to intercalate into the small rhombic tunnels of $Na_2Ti_6O_{13}$. At higher concentrations of Li^+, they occupy sites in the big quasi-rectangular tunnels as it was discussed in the structure analysis before (Figure 1D). They also determined that diffusion in these larger tunnels is limited, with an energetic barrier of 1.4 eV. From the differential capacity curves for this sample (Figure 5C), obtained at different points in the electrode cycle life, it is clear that the responsible for the capacity fade is the process at lower potentials, as proposed by R. Dominko *et al*. (13). The intensity of the cathodic peak does not seem to be modified by the aging of the electrode in contrast with the anodic peak, which decreases significantly from the first to the 28th cycle. We can relate this effect with the previous calculations by Y. Wang *et al.* (20), where Li^+ ions are being incorporated in the big tunnels at higher inserted amount of lithium, but do not have the sufficient energy to de-insert.

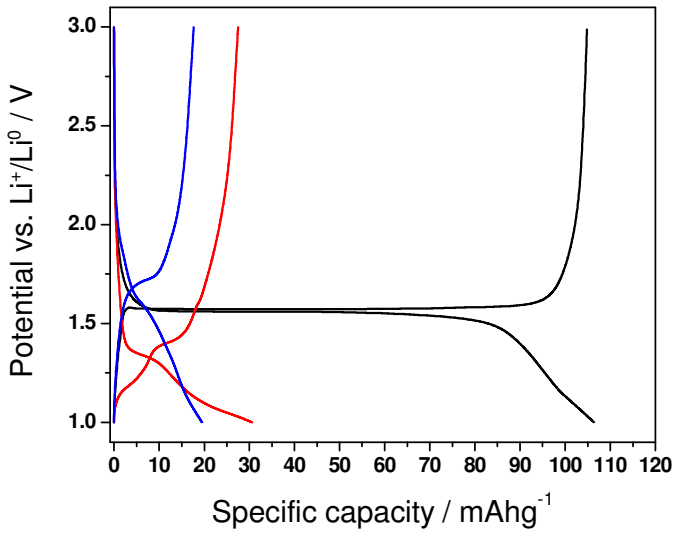

Figure 4. Galvanostatic charge-discharge curves for the three samples at the tenth cycle. Black: $Li_4Ti_5O_{12}$, Blue: $Na_2Ti_3O_7$ and Red: $Na_2Ti_6O_{13}$.

Figure 5D shows the percentage of discharge capacity retention as a function of the number of cycles performed on the three electrode materials. The $Na_2Ti_3O_7$ electrode presented the lowest discharge capacity retention for the three studied electrodes, dropping to 40% of its initial capacity at the 28th cycle.

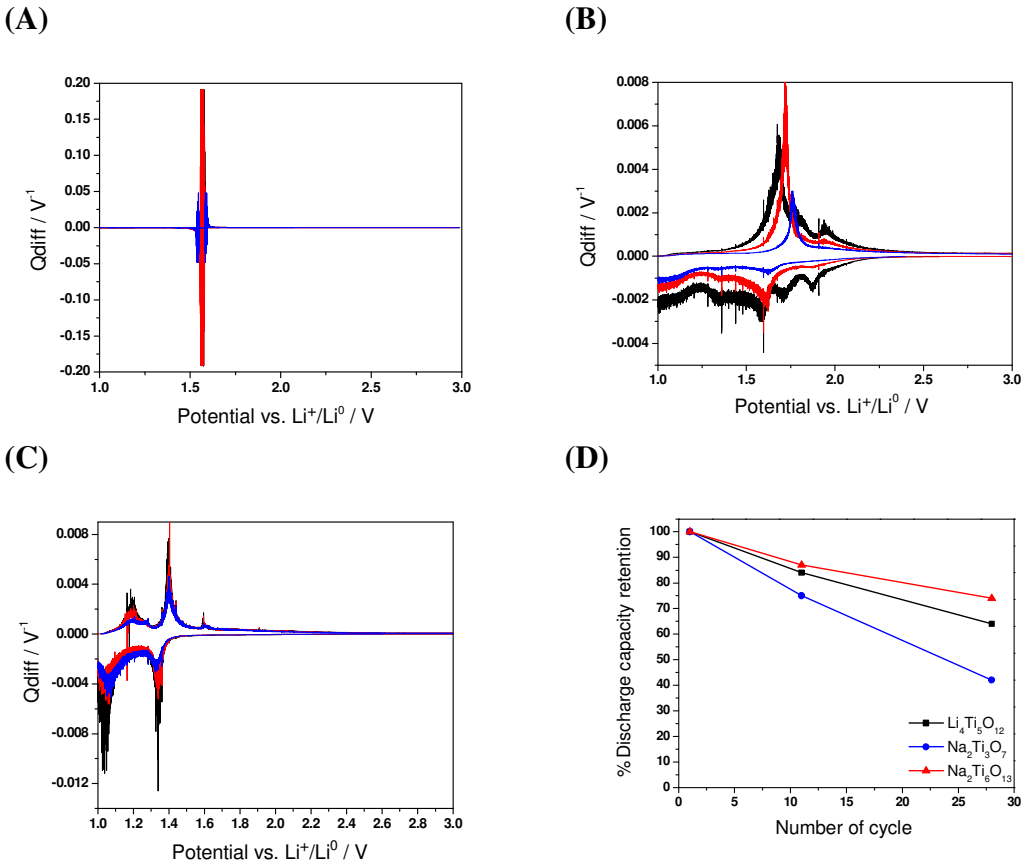

Figure 5. Differential capacity (Q_{diff}) as a function of cell voltage curves for C/2 constant-current charge and discharge tests for (A) $Li_4Ti_5O_{12}$, (B) $Na_2Ti_3O_7$ and (C) $Na_2Ti_6O_{13}$ at the 1st cycle (black), 11th cycle (red) and the 28th cycle (blue). (D) Percentage of the discharge capacity retention at the cycles used to plot the differential capacity curves for the three electrodes.

The kinetic properties of the anode materials were examined by cyclic voltammetry at different scan rates, as shown in Figure 6, with the finding that the profile of the CV response presented a variety of behaviors, depending on the material tested. The absolute current values obtained in the CV experiments for each electrode were converted to current density values making an estimation of the total surface area of the active material deposited on the substrate. From the theoretical gravimetric density and the representative particle size for each titanate compound (previously mentioned), and with the active mass deposited in each electrode, it was possible to estimate the following total surface areas of active material, in cm^2: 2.50 for $Li_4Ti_5O_{12}$, 1.57 for $Na_2Ti_6O_{13}$, and 0.54 for $Na_2Ti_3O_7$.

The shape of the current peaks obtained in the voltammetric experiment (current density-potential curve) gives an insight into the electrochemical kinetics of Li^+ ion insertion/de-insertion occurring together with the $Ti^{IV} \rightarrow Ti^{III}$ (or $Ti^{III} \rightarrow Ti^{IV}$) conversion in

the electrode active material. Sharp and well-defined peaks correlate with a fast electrochemical process occurring at aspecific electric potential. On the other hand, a broad response in the current profile reveals a more complex process involving multiple energy sites and/or slower kinetic characteristics. This was the case for the voltammograms obtained with both sodium titanates, particularly for the cathodic Li^+ ion insertion process, while the CV curve for lithium titanate reveals other different and interesting features. The $Li_4Ti_5O_{12}$ anode shows a highly reversible process, indicated by the shape of the peaks and by the small difference between the potentials of the cathodic and anodic current peaks (100 mV at 0.05 mV s^{-1}). In addition to sharp cathodic and anodic current peaks, the $Li_4Ti_5O_{12}$ material shows an almost linear increase in current density at the onset of both current peaks. These features allow us to infer an electrochemical insertion/de-insertion processes limited by a resistive step, extending up to reach the maximum current density. Simulations in the literature assuming film formation under ohmic resistance control strongly resemble the CVs of Figure 6A (21). This behavior may be contrasted with that expected for processes limited by activated charge transfer or by mass transport, where a quasi-exponential increase of the current with potential is expected. However, it is important to notice that the ohmic behavior evidenced as a resistive slope in the anodic peak for all scan rates analyzed, could be related also with a passivating film at the surface of the anode.

The $Na_2Ti_3O_7$ anode presents a well-defined anodic peak while in the cathodic scan a broad peak is observed that can be associated with lithium insertion. Two shoulders are also evident, related with other cathodic processes. Meanwhile, the $Na_2Ti_6O_{13}$ is the only anode substrate that shows two anodic peaks (better resolved at lower scan rates), indicating that two processes of lithium de-insertion are taking place at two different potentials, which is in agreement with the two plateaus observed in the galvanostatic charge/discharge curves. It is important to notice that there are two small peaks at 1.7 and 1.1 V, associated with other redox processes that could be related to catalytic surface reactions, such as the decomposition of the $LiFP_6$ electrolyte (11). Since the galvanostatic charge and discharge curves were recorded at low currents, equivalent to those obtained in the CV experiment at lower scan rates, we associated this peak to the lower potential plateau. As it can be observed from CV curves, both sodium titanates show an important contribution of the faradaic pseudocapacitance.

For all titanates studied, the peak potential of the Ti^{4+}/Ti^{3+} redox couple observed with CV at the lowest scan rate corresponded adequately with the insertion potential of the galvanostatic charge-discharge curves for each electrode. When the scan rate is increased, the cathodic peak is shifted towards lower potential and the anodic peak to higher potentials. This indicates that at higher scan rates the redox process becomes more irreversible, not allowing the processes of insertion and de-insertion of lithium ions into the host matrix, to be fully completed. This can be correlated with the rate capability results (Figure 7), where the discharge capacity of the electrodes fades, as the discharge current is increased.

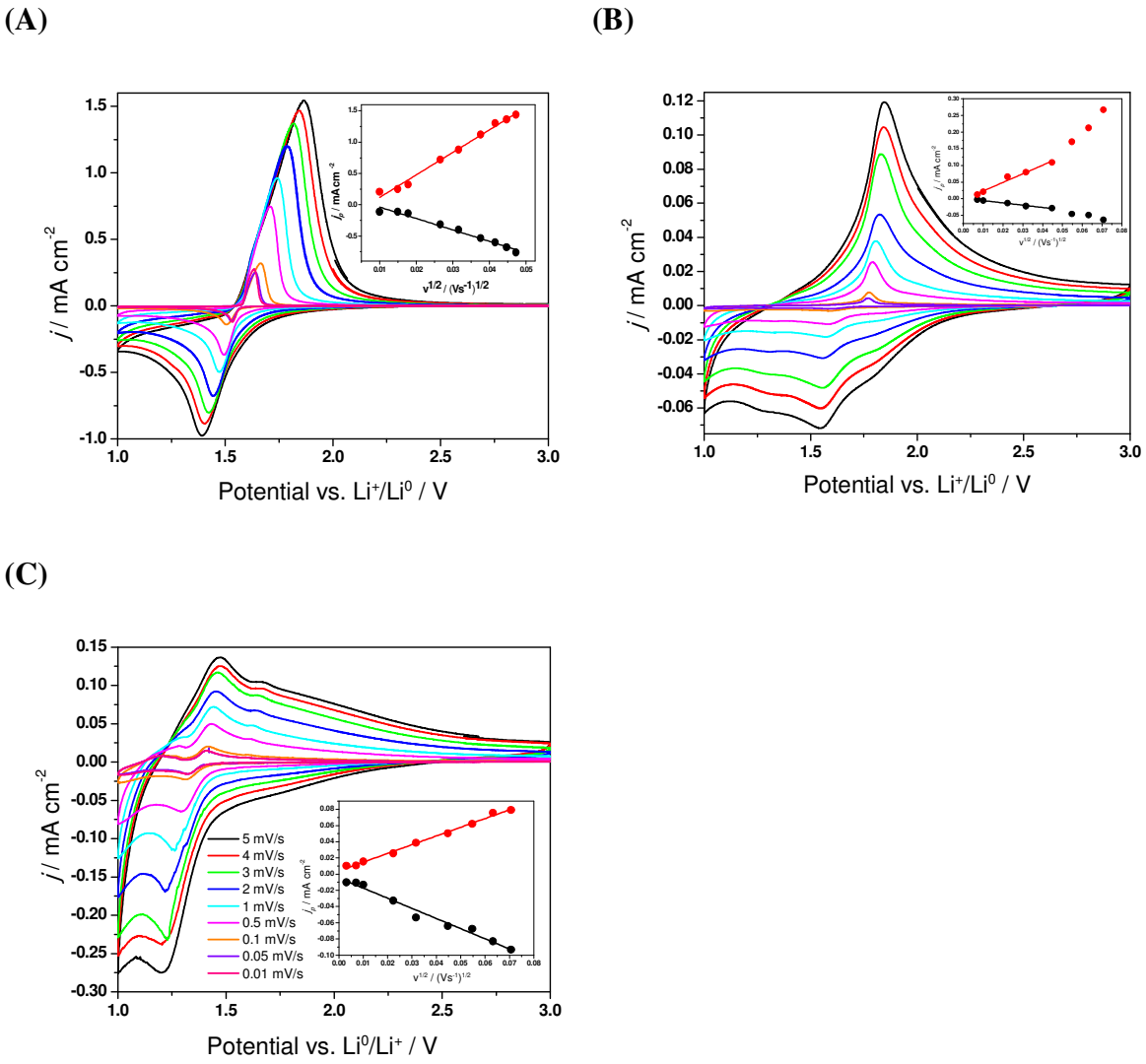

Figure 6. CV curves for the three samples: (A) $Li_4Ti_5O_{12}$ (B) $Na_2Ti_3O_7$ and (C) $Na_2Ti_6O_{13}$, between 3.0 and 1.0 V at different scan rates. Current density, j, was calculated using the total surface area for each active material determinates as described in the text. The color reference for scan rate values is located in C. The inset shows the dependence ofthe anodic (red data points) and cathodic (black data points) peak current density on the square root of the scan rate.

In order to analyze the kinetic behavior of the active materials, we analyzed the dependence of the peak current density, (j_p) on the scan rate (v). If the reactions kinetic is controlled by a diffusional step, the oxidation and reduction currentat the peak should show a linear dependence onthe square root of the scan rate, $v^{1/2}$ (9):

$$j_p = 2.69x10^5 n^{3/2} C_0 D^{1/2} v^{1/2} \quad [5]$$

In equation [5], n is the number of electrons involved in the redox reaction (1 electron for each Ti^{IV} center), C_0 is the bulk concentration of Li^+ (in mol cm^{-3}), D is the diffusion coefficient (in cm^2 s^{-1}) and v is the scan rate (in V s^{-1}). The insets in Figure 6 show the

relationship between j_p and $v^{1/2}$ for each electrode. $Li_4Ti_5O_{12}$ and $Na_2Ti_6O_{13}$ present a linear relationship between both variables, indicating that the process is controlled by diffusion in the range of scan rates studied. Meanwhile, $Na_2Ti_3O_7$ follows a linear relationship at lower scan rates, but at higher scan rates (from 2 mV s^{-1}) it shows mainly a linear dependence with v (data not shown). This phenomenon is observed when there is a mixed controlled process of diffusion and adsorption. From the slope value of the linear relationship of j_p vs. $v^{1/2}$, we were able to calculate the apparent diffusion coefficient of lithium (D_{Li^+}) in the matrix of the anodes (Table II). $Li_4Ti_5O_{12}$ presents a larger D_{Li^+}, indicating that diffusion of ions is faster in this host material than in the other electrodes.

This observation correlates with the rate capability results, where $Li_4Ti_5O_{12}$ is the electrode that has the lowest loss in discharge capacity when the discharge current is increased, since the discharge process delivers lithium ions faster than the other electrodes, even at high anodic currents.

TABLE II. Li^+ diffusion coefficients for the cathodic (D_{Li^+cath}) and anodic (D_{Li^+an}) processes obtained from CV experiments.

Sample	D_{Li^+cath} ($cm^2\ s^{-1}$)	D_{Li^+an} ($cm^2\ s^{-1}$)
$Li_4Ti_5O_{12}$	1.35×10^{-9}	5.11×10^{-9}
$Na_2Ti_3O_7$	6.69×10^{-12}	9.19×10^{-11}
$Na_2Ti_6O_{13}$	2.16×10^{-11}	1.58×10^{-11}

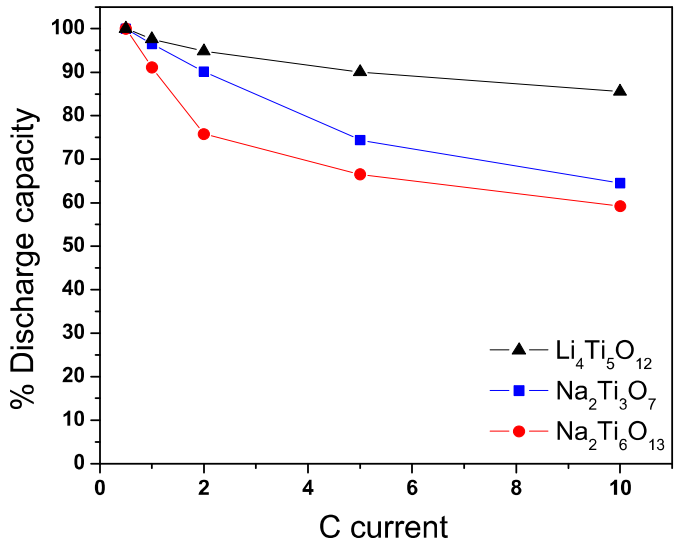

Figure 7. Rate capability tests for the three samples charged at constant current C/2 and discharged at different rates.

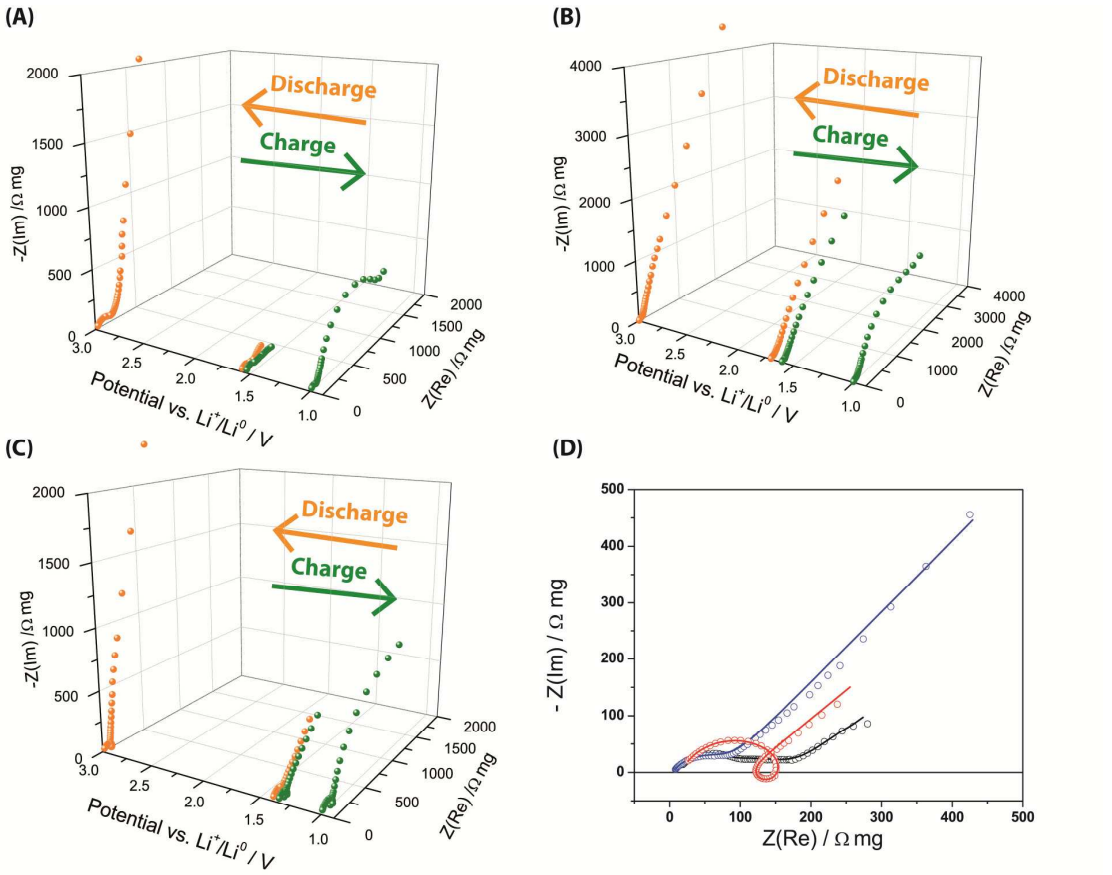

Figure 8. EIS experiments recorded at different states of charge (green) and discharge (orange) for (A) $Li_4Ti_5O_{12}$, (B) $Na_2Ti_3O_7$ and (C) $Na_2Ti_6O_{13}$. The Nyquist plots and theoretical fits for 50% SOD of all samples are plotted in (D), where the original data are represented by dots and the fit by lines. Color code: black: $Li_4Ti_5O_{12}$, blue: $Na_2Ti_3O_7$ and red: $Na_2Ti_6O_{13}$. All the EIS results are normalized according to active material mass for each electrode.

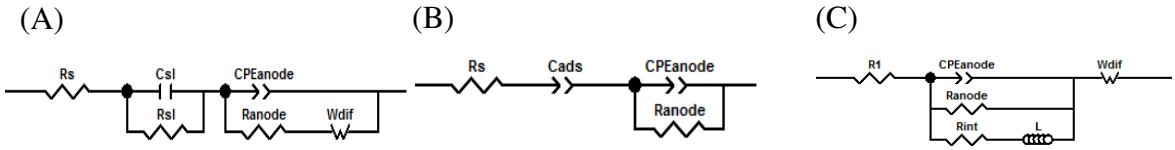

Figure 9. Equivalent electric circuits used for the theoretical fit of the EIS data for 50% SOD: (A) $Li_4Ti_5O_{12}$, (B) $Na_2Ti_3O_7$ and (C) $Na_2Ti_6O_{13}$.

To understand the improved reversible capacity of $Li_4Ti_5O_{12}$ with respect to the sodium titanates, EIS of the three samples were measured and theoretically fitted with software Zview 3.2. Figure 8 (A-C) shows the results of EIS experiments, as Nyquist diagram, performed at different potentials corresponding to the different states of charge (SOC) and discharge (SOD) for the three electrodes. The EIS results presented in green data points corresponds to the measurements performed during the charge and the orange ones belong to the discharge process. In all samples, the potential at 1.0 V represents 100% SOC, 3.0 V represents 100% SOD and the intermediate potentials correspond to the plateau observed in the galvanostatic curves for each titanate. In general, it is observed that when the electrodes are fully charged (100% SOC) the general impedance

of the cell is greatly increased compared to the 50 % SOC, and diffusion is absent in the range of frequencies studied. This phenomenon is expected, since at this stage the matrix is fully loaded and further entrance of Li^+ ions is not allowed. When the discharge process takes place, it is clearly observed the diffusion process, since we are extracting Li^+ ions from the host matrix.

Figure 8D shows the Nyquist diagram for the three electrodes at the 50% SOD fitted with the equivalent circuits shown in Figure 9. Since EIS results showed different behavior and did not respond to a unique equivalent circuit, different models were used to fit each anode material. The equivalent circuit showed in Figure 9A fitted the EIS response of $Li_4Ti_5O_{12}$ in the whole frequency range. Where R_s represents the contact resistance among current collector, electrode and electrolyte, C_{sl} and R_{sl} are the capacitance of the surface layer formed between electrolyte and the anode respectively, corresponding to the semicircle at high frequencies. At intermediate frequencies, CPE_{anode} and R_{anode} are associated to the constant phase element and the resistance, respectively, corresponding to the charge-transfer impedance of Li^+ ions in the anode matrix. Finally W_{dif} is a Warburg element corresponding to diffusion transport for electroactive species (Li^+ ion diffusion). For $Na_2Ti_3O_7$ the equivalent circuit is showed in Figure 9B. In this case, only one semicircle can be observed in the Nyquist plot in the Figure 8D and correspond to the electric circuit with a CPE_{anode} and R_{anode} in parallel, as previously described for the $Li_4Ti_5O_{12}$ anode. C_{ads} represents a capacitive contribution that we associate to a mechanism of Li^+ ion adsorption on the surface of the active material. The adsorptive behavior in this material was also detected by CV experiments at the highest scan rates, as was previously discussed (linear response of j_p vs. v). For $Na_2Ti_6O_{13}$ an inductive loop was detected in the 10-100 Hz frequency range, and is represented by L in the equivalent circuit shown in Figure 9C. All the remaining elements are the same as mentioned in the previous circuits. To the best of our knowledge, this particular behavior has not been previously reported for this material. Inductance is commonly related to the adsorption of negatively charge species (22). We associate this effect to the presence of F^- ions that may have appeared as a result of parasitic reactions in the electrolyte. This catalytic effect was proposed by R. Dominko *et al.* (13), which now we confirm with EIS results as well as CV and GCD experiments.

Conclusions

We presented a morphological and electrochemical characterization of different alkali metal titanates ($Li_4Ti_5O_{12}$, $Na_2Ti_3O_7$ and $Na_2Ti_6O_{13}$) as active anode materials for lithium-ion batteries. We have succeeded in the synthesis of the three alkali metal titanates proposed with high purity and crystallinity, as inferred from XRD, Raman spectroscopy and SEM measurements. From the GCD experiments, all the titanate showed lithium storage. It was observed high lithium storage capacity (up to 110 mAh g^{-1}) for $Li_4Ti_5O_{12}$. Although a resistive effect was observed in the CV experiments, probably due to the growth of a resistive film, this electrode showed the best rate capability results and faster Li^+ ion diffusion into the host matrix. Thus, this compound resulted to be the most promising of all three titanates samples studied as active anode material. We attribute this faster diffusion due to its more open structure, observed by X-ray diffraction experiments. From EIS it is observed that, all the titanate materials can be fitted with an equivalent electric circuit consisting of at least one RC-type circuit (two RC

type sub-circuits for $Li_4Ti_5O_{12}$). A Warburg element was present at low frequencies for all the electrodes at 50% SOD or 50% SOC. The $Na_2Ti_6O_{13}$ material showed an inductive loop at intermediate frequency range in all states of charge/discharge which could be associated with surface catalytic reactions of electrolyte ions (this feature will be subject of further studies).

Acknowledgments

This research was supported by CONICET Argentina (PIP 11220110100992) and SECyT-UNC. S.Ch. and C.B.R. acknowledge for fellowship given by CONICET. We would like to thank Dr. Elisa Pannunzio for her insightful assistance with XRD analysis. E.P.M.L. thanks Program BID (PICT 2012-2324).

References

1. M. Armand and J. M. Tarascon, *Nature*, **451**, 652 (2008).
2. C. B. Robledo, J. E. Thomas, G. L Luque, E. P. Leiva, O. R. Cámara, D. Barraco, A. Visintin, *Electrochim. Acta*, **140,** 160 (2014).
3. C. Robledo, M. Otero, G. Luque, O. Cámara, D. Barraco, M. I. Rojas, E. P. M. Leiva, *Electrochim. Acta*, **140,** 232 (2014).
4. C. P. Sandhya, B. John and C. Gouri, *Ionics (Kiel).*, **20**, 601 (2014).
5. T. Yuan, X. Yu, R. Cai, Y. Zhou and Z. Shao, *J. Power Sources*, **195**, 4997 (2010).
6. H. Zhang, G. R. Li, L. P. An, T. Y. Yan, X. P. Gao and H. Y. Zhu, *J. Phys. Chem. C*, **111**, 6143 (2007).
7. R. Armstrong, G. Armstrong, J. Canales and P. G. Bruce, *J. Power Sources*, **146**, 501 (2005).
8. D. P. Singh, F. M. Mulder and M. Wagemaker, *Electrochem. commun.*, **35**, 124 (2013).
9. W.-H. Ryu, D.-H. Nam, Y.-S. Ko, R.-H. Kim and H.-S. Kwon, *Electrochim. Acta*, **61**, 19 (2012).
10. S. Huang, Z. Wen, Z. Gu and X. Zhu, *Electrochim. Acta*, **50**, 4057 (2005).
11. S. Papp, L. Kõrösi, V. Meynen, P. Cool, E. F. Vansant and I. Dékány, *J. Solid State Chem.*, **178**, 1614 (2005).
12. E. Bamberger and M. Begun, *J. Am. Ceram. Soc.*, **70**, 48 (1987).
13. R. Dominko, E. Baudrin, P. Umek, D. Arčon, M. Gaberšček and J. Jamnik, *Electrochem. commun.*, **8**, 673 (2006).
14. W. Liu, Y. Wang, X. Jia and B. Xia, *J. Chem.*, 1 (2013).
15. C. P. Sandhya, B. John and C. Gouri, *J. Mater. Sci.*, **48**, 5827 (2013).
16. Y. Su, M. Lou Balmer and B. C. Bunker, *J. Phys. Chem. B*, **104**, 8160 (2000).
17. H. Thompson, *J. Electrochem. Soc.*, **126**, 608 (1979).
18. X. Han, M. Ouyang, L. Lu, J. Li, Y. Zheng and Z. Li, *J. Power Sources*, **251**, 389 (2014).
19. J. C. Pérez-Flores, F. García-Alvarado, M. Hoelzel, I. Sobrados, J. Sanz and A. Kuhn, *Dalton Trans.*, **41**, 14633 (2012).
20. Y. Wang, H. Zhang, X. Yao and H. Zhao, *ACS Appl. Mater. Interfaces*, **5**, 1108 (2013).

21. A. J. Calandra, N. R. D. E. Tacconi, R. Pereiro and A. J. Arvia, *Electrochim. Acta*, **19**, 901 (1974).
22. P. Acevedo-Peña and I. González, *J. Solid State Electrochem.*, **16**, 2709 (2012).